

Interaction of Saturn's Hexagon with convective storms

A. Sánchez-Lavega^{1,*}, E. García-Melendo², T. del Río-Gaztelurrutia¹, R. Hueso¹, A. Simon³, M.H. Wong⁴, K. Ahrens-Velásquez², M. Soria², T. Barry⁵, C. Go⁶, C. Foster⁷

¹ Departamento Física Aplicada I, Escuela de Ingeniería de Bilbao, Universidad del País Vasco UPV/EHU, Bilbao, Spain.

² Universitat Politècnica de Catalunya UPC, Terrasa, Spain

³ NASA Goddard Space Flight Center/690, Greenbelt, MD, USA

⁴ University of California, Berkeley, CA, USA

⁵ Broken Hill Observatory, Broken Hill, Australia

⁶ University of San Carlos, Cebu, Philippines

⁷ Astronomical Society of Southern Africa, Centurion, South Africa

Corresponding author: Agustín Sánchez-Lavega (agustin.sanchez@ehu.eus)

Key Points:

- Following an outbreak of polar storms in 2018, we observed in March-May 2020 a new episode of storms south of Saturn's hexagonal wave.
- The storms did not produce a noticeable change in the zonal wind profile in the polar area.
- The hexagon shape was perturbed after the storms but the wave suffered **no** change in its rotation period matching that of System III.

35 Abstract

36

37 In March 2020 a convective storm erupted at planetographic latitude 76°N in the southern flank
38 of Saturn's long-lived hexagonal wave. The storm reached a zonal size of 4,500 km and developed
39 a tail extending zonally 33,000 km. Two new short-lived storms erupted in May in the hexagon
40 edge. These storms formed after the convective storms that took place in 2018 in nearby
41 latitudes. There were no noticeable changes in the zonal profile of Saturn's polar winds in 2018-
42 2020. Measurements of the longitude position of the vertices of the hexagon throughout this
43 period yield a value for its period of rotation equal to that of System III of radio-rotation measured
44 at the time of Voyagers. We report changes in the hexagon clouds related to the activity of the
45 storms. Our study reinforces the idea that Saturn's hexagon is a well rooted structure with a
46 possible direct relationship with the bulk rotation of the planet.

47

48

49 Plain Language

50

51 Convective storms of zonal extent greater than 4,000 km are rare in Saturn's atmosphere. They
52 occur every few years, and exceptionally, (perhaps once every 20-30 years) they reach 10,000 km
53 and become a Great White Spot that expands along an entire latitudinal band of the planet. In
54 2018, multiple eruptions of medium-sized storms occurred close to the North Polar Region. After
55 a period of calm throughout 2019, new eruptions took place in 2020, at 76°N latitude on the
56 border of the hexagon wave, the closest to the pole ever observed. These storms changed the
57 morphology of the clouds in the region, but the hexagon itself was not affected in its motion or
58 dynamics, with no change in the zonal winds. This, together with its longevity, indicates that the
59 hexagon is a robust meteorological formation. Its rotation period in these years remained that of
60 the System III radio rotation measured by the Voyager spacecraft, reinforcing the idea of its
61 possible direct relationship with the bulk rotation of the planet.

62

63 1 Introduction

64

65 From March to August 2018 four outbreaks of convective storms took place sequentially
66 at planetographic latitudes from 66.7°N to 74.7°N , disturbing a whole latitude band spanning a
67 width of $\sim 8,000$ km [Sánchez-Lavega et al., 2020]. Subsequently and throughout 2019, no new
68 storms occurred, although the entire region between latitudes 66°N and 75°N presented
69 numerous spots and white and dark areas (in visible wavelengths) difficult to track due to their
70 low contrast and variability in short time scales (Figure S1). On March 25, 2020, a new convective
71 outbreak started with a sudden bright spot (Figure 1) northwards of the 2018 events, on the edge
72 of Saturn's hexagonal wave at 79°N where the wind profile turns anticyclonic [Sánchez-Lavega et
73 al., 2014; Antuñaño et al., 2015; Sayanagi et al., 2019]. Later in May of 2020, two other short-
74 lived storms emerged, this time even further north on the southern flank of the hexagon. Two
75 aspects of this phenomenon are of interest. On one hand, the convective storms themselves, due
76 to their size and brightness (and energy involved), have never been reported before at polar
77 latitudes in Saturn. On the other hand, their location next to the hexagon, which allows the study
78 of their interaction with this enduring wave, provides new information about the hexagon itself,

79 in particular regarding its stability, robustness and longevity when subjected to nearby severe
80 disturbances. Finally, we explore if the extensive and intense convective activity in 2018 and 2020
81 had an effect on Saturn’s zonal wind profile at these latitudes.

82

83 2 Observations

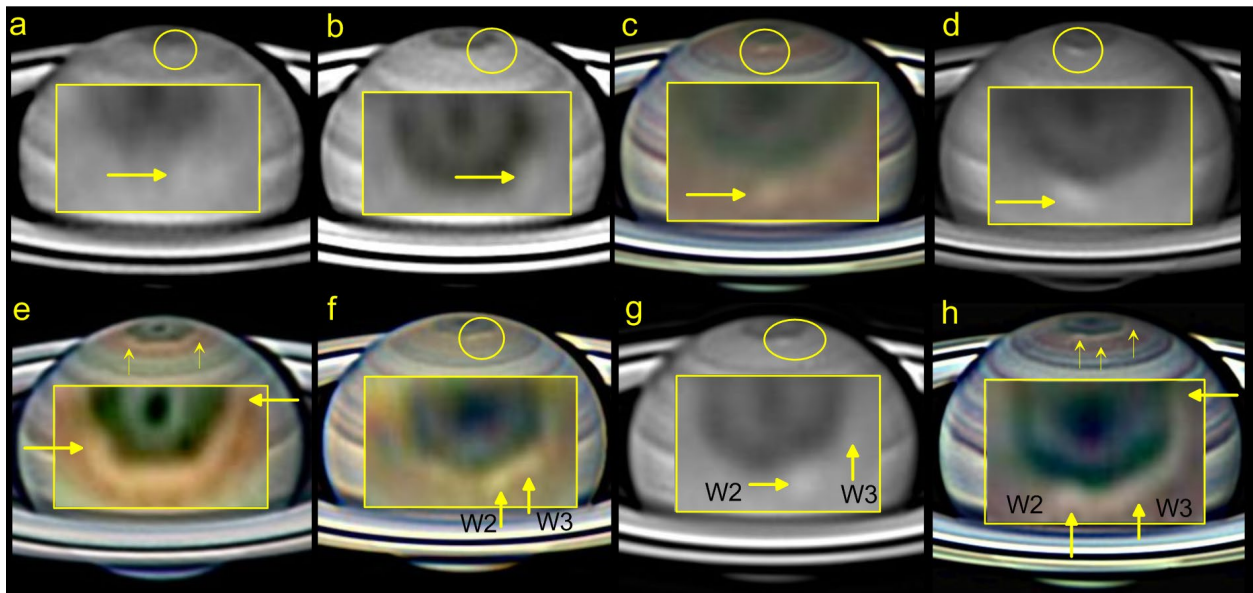
84

85 For this study we used two sets of data: (1) Images obtained using the “lucky imaging”
86 methodology in the spectral range 380-950 nm by a large number of observers distributed
87 around the world using telescopes of 30-50 cm in diameter (see Supporting Information). These
88 images provide a continuous survey with a nearly daily coverage of Saturn during the apparitions
89 in the years 2018 (from 23 March to 21 November, opposition 27 June), 2019 (from 27 February
90 to 28 October, opposition 9 July) and 2020 (25 March – 10 October, opposition 20 July). In total,
91 we navigated and measured about ~ 560 images selected among the ~ 3,000 images for years
92 2019-2020 submitted to the PVOL image database [Hueso et al., 2018] and to the ALPO-Japan
93 web site (see Supporting Information). Most images are either color RGB composites or red-to
94 near-infrared images in the wavelength ranges ~ 650-950 nm and 750-950 nm. They have a
95 spatial resolution ~ 600 – 900 km in the disk under the best seeing conditions; (2) Hubble Space
96 Telescope (HST) images obtained as part of the OPAL program [Simon et al., 2015] in one visit
97 per year close to the opposition (6-7 June 2018, 19-20 June 2019, 4-5 July 2020). These images
98 were obtained with the Wide Field Camera 3 (WFC3) using filters F225W, F275W, F343N, F395N,
99 F467M, F502N, F631N, F658N, FQ727N (methane absorption band), F763M, and FQ889N
100 (methane absorption band). Details of the image analysis is given in [Sánchez-Lavega et al., 2020]
101 and in Supporting Information.

102

103

104



105

106

107

108 **Figure 1.** *Ground-based images of the convective storms in 2020. The storms are identified on the*
109 *disk by circles and arrows to indicate their zonal expansion. The inset shows a polar projection of*
110 *the storms and the hexagon. Storm W1 is visible in (a) March 25, red, C. Foster; (b) March 29, red,*
111 *C. Foster; (c) April 11, RGB, C. Go; (d) April 12, red, N. MacNeill; (e) April 15, RGB, D. Peach, where*
112 *the storm expands eastward. Storms W2 and W3 are shown in (f) May 1, RGB, T. Oliveti; (g) May*
113 *3, red, M. L. G. Wong; (h) May 5, RGB, C. Go, with storm W3 expanding eastward.*

114 115 **3. Storm activity and the zonal wind profile**

116
117 The first polar storm of 2020 (W1) was captured on March 25 2020 at latitude 74°N at red
118 wavelengths as a faint bright spot ~ 4,000 km wide (Figure 1a). The following days the spot kept
119 the same aspect (Figure 1b-c), and 4 days after outbreak, on March 29, it had expanded zonally,
120 forming a tail that by April 11 reached ~ 17,000 km east of its head (Fig. 1d). We interpret this
121 tail as the expansion of the storm clouds by winds blowing eastward relative to the actively-
122 convecting plume-head with a velocity of 11 ms⁻¹ (or 3.3 ms⁻¹ in System III). In April 15 the storm
123 head had a size of 5,400 ± 500 km, penetrating into the hexagon up to latitude 79.5°N (or 1,270
124 km into the south side of the hexagon) (Figure 1e). At that date, the tail of white clouds
125 surrounded the hexagon, extending at least 39,200 km east of the head. This implies an eastward
126 expansion by the winds relative to the head with a velocity of 21 ms⁻¹ (or 14 ms⁻¹ in System III).
127 Figure 2a shows our measurements of the drift of the head of the storm in System III longitude
128 and in Table 1 we give the velocity values, which fit well Saturn's wind profile at these latitudes
129 [Sánchez-Lavega et al., 2000; García-Melendo et al., 2011]. Figure 2b shows that W1 migrated ~
130 2.3° (~ 2,600 km) northwards of its onset position, towards the hexagon edge. The meridional
131 velocity resulting from a linear fit to this drift was +1.2 ms⁻¹.

132
133 On May 1, two other bright spots (W2 and W3) were detected (Figure 1f-g-h). We consider
134 them as new outbreaks arising in the expanding tail of the main storm W1, which was no longer
135 visible on this date. The onset of W2 took place 2,250 km east of the expected position of W1,
136 and W3 emerged 9,250 km further east of W2 (Figure 1f). Both spots were located northward by
137 0.7° of W1 and moved faster, (Figure 2a and Table 1) in agreement with the wind profile (Figure
138 2c). They were located on the anticyclonic side of the eastward jet embedded in the hexagon,
139 thus interacting with it. From May 3 to August 1 we detected about 40 diffuse white spots at
140 latitudes 75.5°N - 77°N, close to the hexagon (Fig. 2a, Fig. S2). Except for an isolated dark spot DS
141 (figure 3b) at 76.6°N ($u = 25 \text{ ms}^{-1}$), the variability and low contrast of these spots makes their
142 identification and tracking difficult, so we did not try to measure their velocities. However their
143 presence indicates that the activity continued on the south side of the hexagon for months after
144 the three main storm outbreaks.

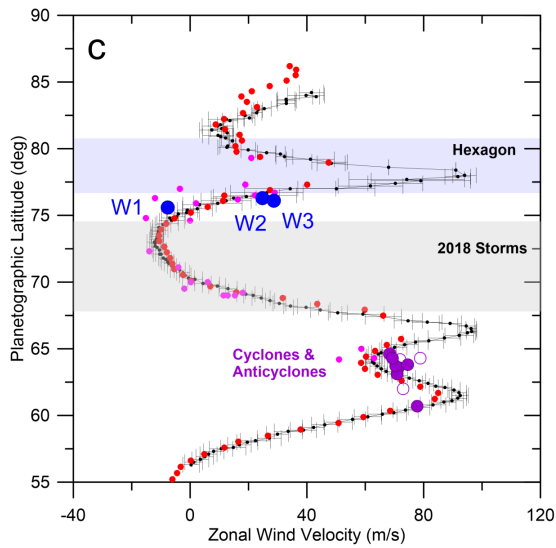
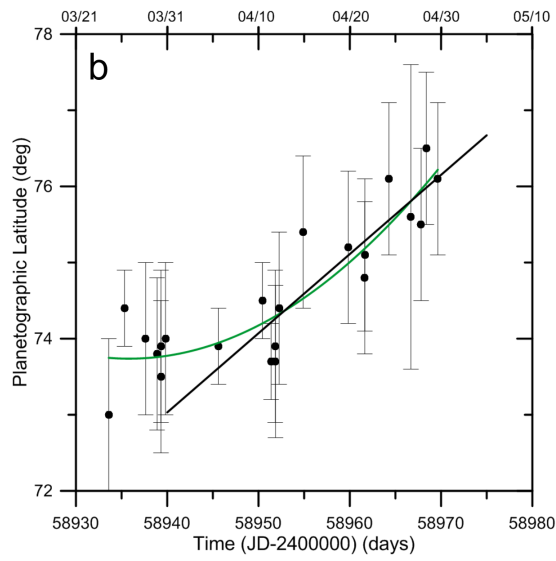
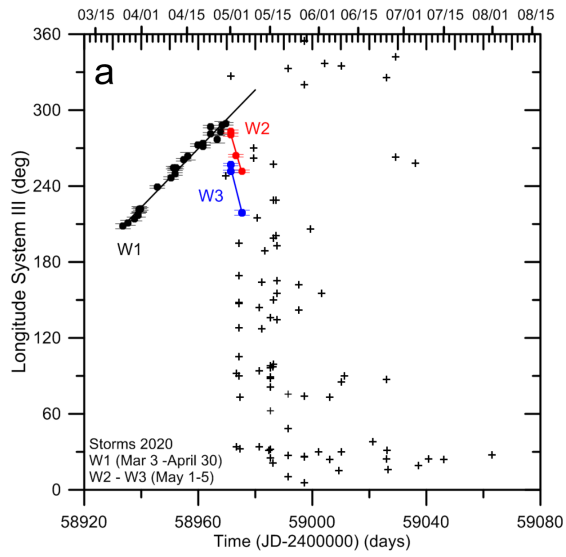
145
146 In order to see if this stormy activity had any influence on the zonal wind profile, we
147 measured the motions of cloud features in the years of interest using different methods. First,
148 we measured the winds in pairs of images from the HST OPAL program separated by one rotation
149 of the planet, using the image correlation velocimetry technique [Hueso et al., 2009, Sánchez-
150 Lavega et al., 2019]. The images selected were obtained in red filters (F631N, F763N) where the
151 contrast of the cloud features is highest. This profile was binned in boxes of 0.5° width in latitude

152 giving velocity errors of 15 ms^{-1} (Simon et al., 2021). Secondly, we performed a manual tracking
 153 of the most significant features in the stormy region using 4-5 HST images with a maximum
 154 coverage over time ($\sim 10 - 14 \text{ hr}$), giving velocity measurements with errors $< 10 \text{ ms}^{-1}$. Finally, we
 155 tracked the most prominent features from ground-based images, a technique that provides very
 156 accurate velocities due to the long temporal coverage (errors $\sim 1 \text{ ms}^{-1}$, Fig. S3-S4). In this last
 157 case, most of the features correspond to spots in the double jet between 60°N and 65°N where
 158 cyclones and anticyclones tend to concentrate [del Rio-Gaztelurrutia et al., 2018]. Their long term
 159 track in 2020 is shown in Fig. 2a, 2b and S3 and the resulting wind profile is shown in Figure 2c.
 160 The long-term track of this kind of spot in 2019 (Fig. S4) and the similarly derived wind profile for
 161 that year are shown in Fig. S4 and S5). A comparison with the velocity profiles measured in 1981
 162 using Voyager images [Sánchez-Lavega et al., 2000] and in 2004-2009 using Cassini images
 163 [García-Melendo et al. 2011] indicates that within measurement uncertainties, the wind profile
 164 was not affected by the storm activity, confirming our previous results for 2018 [Sánchez-Lavega
 165 et al., 2020].

166
 167 **TABLE 1**
 168 **Motions of the convective storms and Hexagon wave vertices**
 169

Feature	Onset (2020)	Latitude $\varphi(^{\circ})$	Drift $\omega (^{\circ}\text{d}^{-1})$	Zonal velocity $u (\text{ms}^{-1})$	Tracking time (d)
W1	25 March	$75.6^{\circ} \pm 1^{\circ}$	2.32	-7.7	36
W2	1 May	$76.3^{\circ} \pm 0.5^{\circ}$	-7.8	24.8	5
W3	1 May	$76.3^{\circ} \pm 0.7^{\circ}$	-8.9	28.7	5
Hexagon 2018	29 Mar – 3 Nov	$78.4^{\circ} \pm 0.3^{\circ}$	$+0.017 \pm 0.024$	-0.046 ± 0.065	219
Hexagon 2019	7 Apr – 28 Oct	$78.4^{\circ} \pm 0.3^{\circ}$	-0.0095 ± 0.018	$+0.026 \pm 0.065$	204
Hexagon 2020	26 Mar - 20 Nov	$78.4^{\circ} \pm 0.3^{\circ}$	-0.008 ± 0.010	$+0.026 \pm 0.063$	229

170
 171



174 **Figure 2.** Motions and velocities of the convective storms in 2020. (a) Drift in System III longitude
175 of storms W1, W2, W3 between 25 March and 5 May 2020. Other smaller and **low-contrast** spots
176 in the latitude range 74°N-76.5°N are identified by crosses (Fig. S2); (b) Drift in planetographic
177 latitude of the center of storm W1. The **green** line corresponds to a degree-two polynomial fit and
178 the **black** line to a linear fit. **In (a) and (b) the date (month/day) is indicated in the upper axis** (c)
179 Zonal wind profile in Saturn's North Polar Region in 2020 relative to System III rotation frame. The
180 red dots are from the correlation velocimetry on HST images (Simon et al., 2021) and magenta
181 dots from major selected features from manual tracking on the same images. The three blue dots
182 identified as W1, W2 and W3 correspond to the three storms. The purple disks and circles are
183 from the tracking of long-lived spots in ground-based images (Fig. S3). The black line and dark
184 dots correspond to the reference wind profile from Cassini ISS measurements [García-Melendo et
185 al., 2011]. The gray areas indicate the latitude band where the 2018 storms evolved **and the**
186 **location of the hexagon.**

187

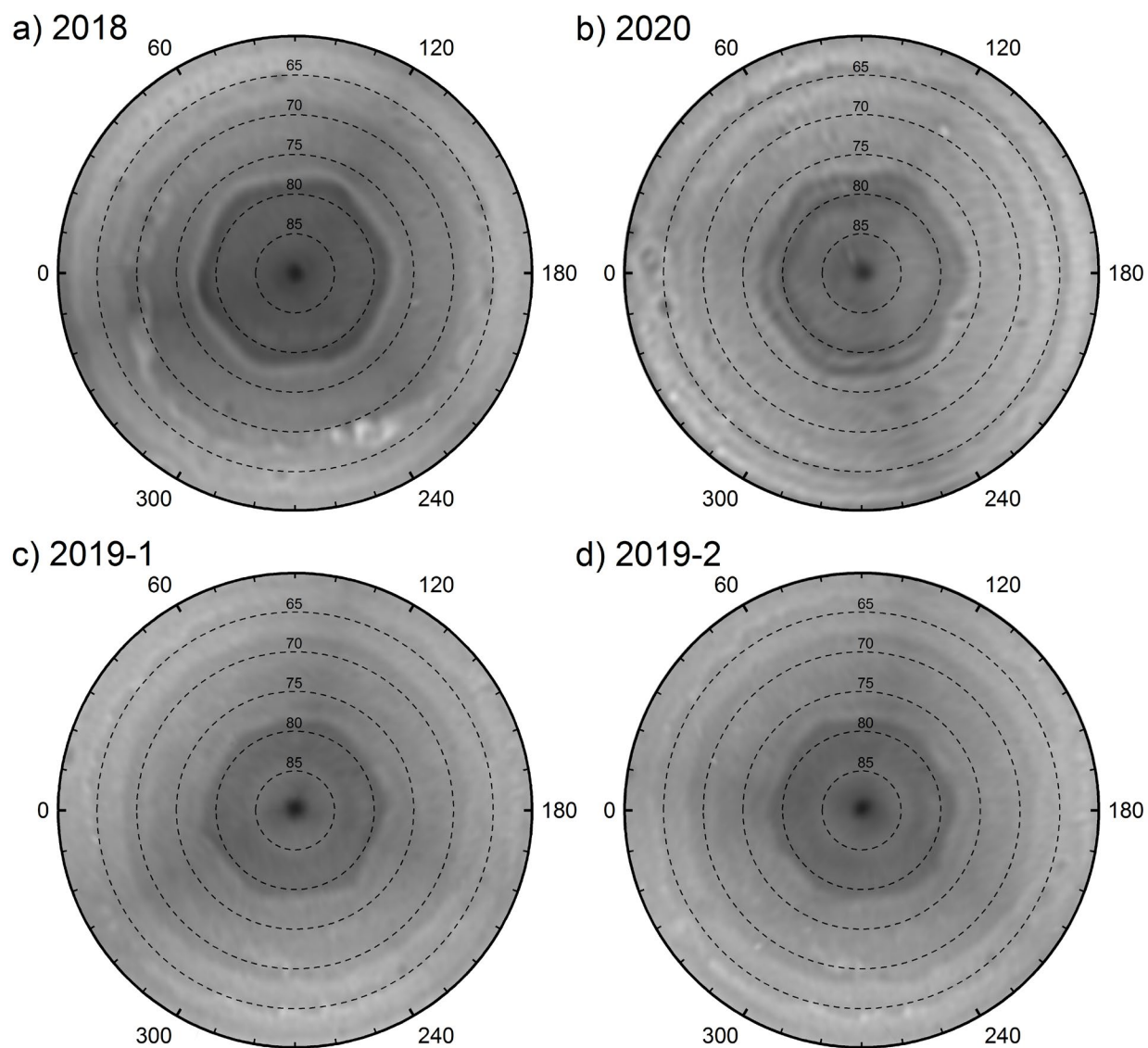
188 **4. The Hexagon wave**

189

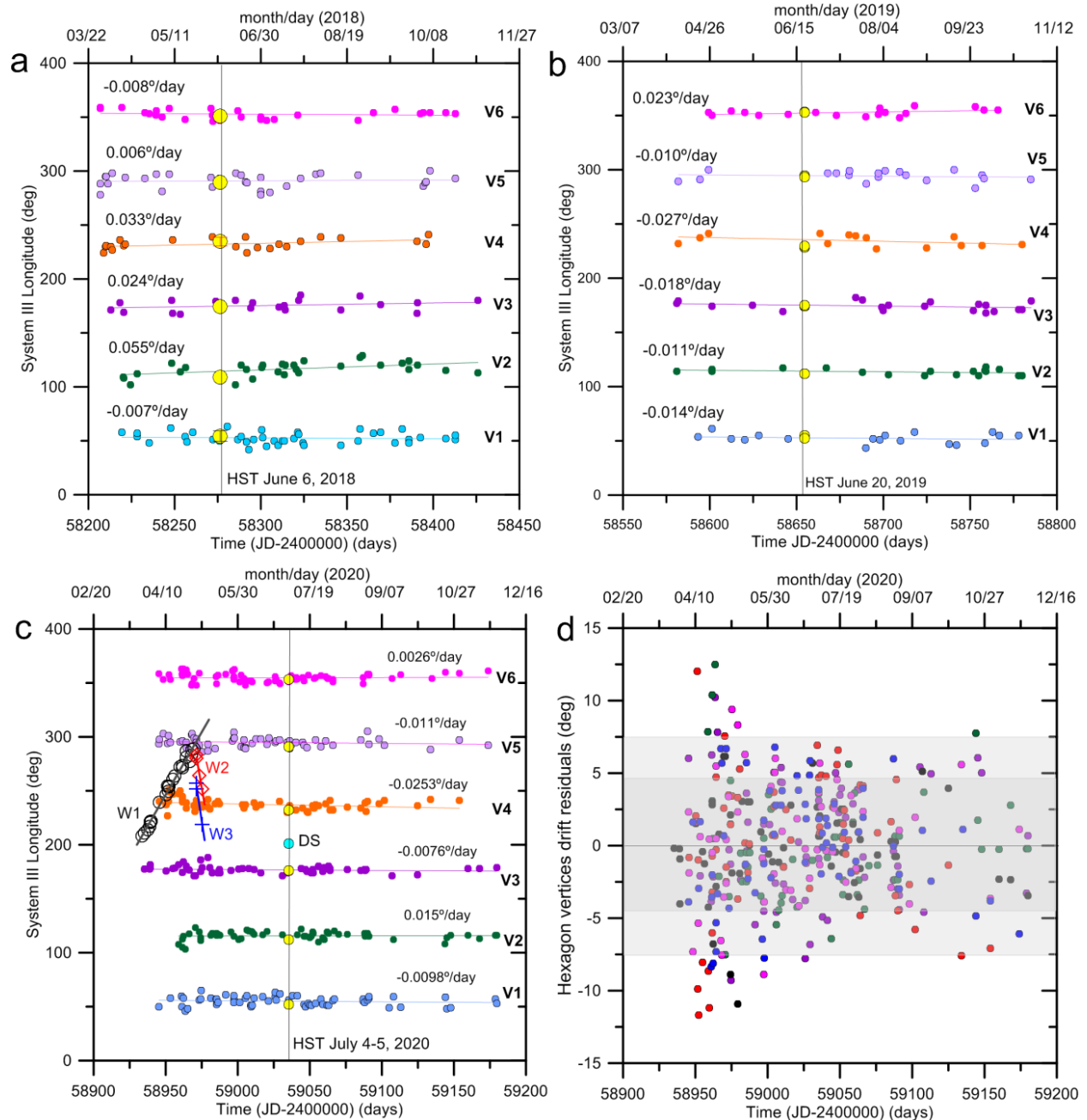
190 The presence of convective storms on the southern flank of the hexagon, and their
191 resulting interaction with it, provides a good test to probe the effects of storms on the wave. In
192 Figure 3, we show composite maps of the polar region using HST OPAL images from years 2018-
193 2020, at a wavelength of 763 nm where the hexagon is usually well contrasted. The vertices of
194 the hexagon are identified as V1 to V6 in Figure 4. In the period 2018-2020 the hexagon clouds
195 [Sanz-Requena et al., 2018] showed changes with respect to their usual sinusoidal distribution
196 [Antuñano et al., 2015]. The eastward jet embedded on the hexagon has peak velocities at 78.3°N
197 and it is usually traced at 763 nm by white clouds, surrounded on the north and south by low
198 albedo belts of varied contrast at ~ 76.5°N and 80.5°N [Antuñano et al. 2015, 2018, Sayanagi et
199 al., 2018]. In 2018 the northern belt and a white zone were very prominent (Fig. 3a), with the
200 transition between them near the peak of the jet. However, in 2019, there was a strong contrast
201 drop in these bands and the hexagon was visible by contrast at the equatorial edge of the
202 northern belt (Figure 3c-d) at about 78.6°N. A faint white zone and a hint of a darker belt are
203 visible south of it. Dark features moving rapidly at the edge of the hexagon changed its regular
204 aspect and made identification of vertices difficult (Fig. 3c-d). These features moved with the
205 **hexagon** eastward jet (Fig. S5). Finally, in 2020 the contrast was recovered, highlighting the two
206 belts enclosing the white band (Fig. 3b). It is tempting to correlate these changes in the clouds
207 with the storm activity in 2018 and 2020.

208

209



210
 211 **Figure 3.** The hexagonal wave from HST images. Composite polar map projections of 763nm
 212 images for the following dates: (a) 6 June 2018 9:54; 6:43 and 12:49 ; (b) 4 July 2020 21:13 and 5
 213 July 2020 0:24 and 3:35 (c) 20 June 2019 00:09; 03:27 and 06:38 (d) 20 June 2019 08:06; 11:16;
 214 14:24 and 17:34. Vertices V1 to V6 are at approximate System III longitudes 60°, 120°, 180°, 240°
 215 300° and 360°. Spot DS can be identified in (b) at longitude 200° and latitude 76.6°.
 216 Planetographic latitudes are indicated by dashed circles.
 217



218
 219
 220
 221
 222
 223
 224
 225
 226
 227
 228

Figure 4. System III longitudes of the vertices of the hexagon along 2018 (a), 2019 (b) and 2020 (c). Vertices identified V1 to V6 are indicated by different colors and yellow dots indicate measurements on HST images. Colored straight lines are linear fits to the position of each vertex, and the value of the drift rate (in degrees/day) is given above the fitted line. In (c) we include the tracks of the convective storms W1, W2, W3 as well as the position of the dark spot DS. (d) Plot of the residuals of the longitude position of the vertices in 2020 relative to the linear fits shown in (c).

229 **5. Numerical simulations of storms**

230

231

232

233

234

235

236

237

238

239

240

241

242

243

244

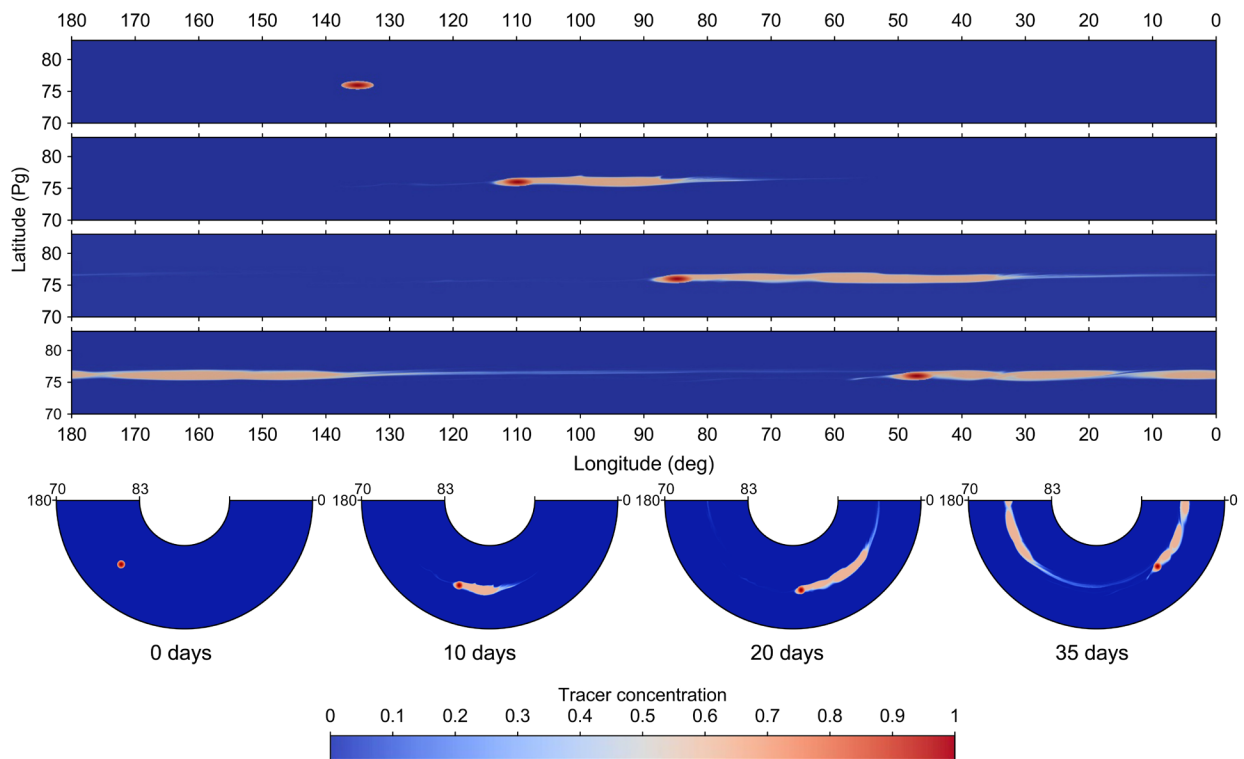
245

246

247

248

We have used a parallelized version of the Shallow Water model (SW) developed by García-Melendo and Sánchez-Lavega (2017) to characterize the intensity of the 2020 storms. In our SW model, we try to reproduce the storm shape and evolution by changing the mass injection rate (Q) that mimics the convective source, its size, and source location on Saturn's wind profile. Details of the simulations are given in Supplementary Information). The SW model produces maps showing the evolution of a material tracer generated by the continuous injection of a mass flow during the whole simulation. In Figure 5 we show the result of a simulation that models the observed storm size and the formation and zonal expansion of an eastward wake. The material tracer is injected at latitude 76°N and the required mass flow is $Q = 5 \times 10^9 \text{ m}^3\text{s}^{-1}$. This value is similar to the value found for the 2018 storms ($Q = 2 \times 10^9 \text{ m}^3\text{s}^{-1}$) [Sánchez-Lavega et al., 2020] and in our preliminary analysis of the mid-latitude storms observed in the northern hemisphere during the Voyager 1 and 2 flybys [Smith et al., 1982; Sromovsky et al., 1983] and in the southern hemisphere with Cassini in 2004-2010 [Dyudina et al., 2007; Baines et al. 2009]. The intensity of all these storms is, however, much lower than the Great White Spots that appeared in 1960 at subpolar north latitudes ($Q = 10^{11} \text{ m}^3\text{s}^{-1}$), in 1990 at equatorial latitudes ($Q = 10^{11}-10^{12} \text{ m}^3\text{s}^{-1}$) and in 2010 at north northern mid-latitude ($Q = 10^{10}-10^{11} \text{ m}^3\text{s}^{-1}$) [García-Melendo and Sánchez-Lavega, 2017; Sánchez-Lavega et al., 2018].



249

250

251

252

253

Figure 5. Shallow Water numerical simulations of the convective storm evolution in Saturn's north polar wind field. The maps (upper cylindrical and lower polar projections) show the material tracer evolution in time for a continuous source with a mass flow $Q = 5 \times 10^9 \text{ m}^3\text{s}^{-1}$ and a size of 5 degrees

254 *in longitude placed at latitude 76°S. Compare the upper map with figure 1a for the initial storm*
255 *aspect and the middle maps at 10 and 20 days with figures 1c and 1d for the eastward expansion*
256 *of the cloud.*

257

258

259 **6. Discussion and Conclusions**

260

261 The new convective storms reported here are the first observed at such high latitude in
262 Saturn. The storms in 2020 erupted at latitude 76.5°N, on the southern side of the hexagonal
263 wave. They appeared northward than those in 2018, thus we are tempted to propose that they
264 are a continuation of the activity that began that year at 67°N and spread north up to 75°N. Their
265 outbreak took place at Saturn's solar orbital longitude $L_s = 121^\circ\text{-}123^\circ$ under high insolation at this
266 latitude (see Figure 6 in Sanchez-Lavega et al., 2020). The SW simulations of the size **of the storms**
267 and evolution indicate that they had comparable intensity to those of 2018, therefore suggesting
268 similar onset conditions in the region. The 2020 storms are also similar in their brightness, size
269 and tail formation, to a storm reported at high latitudes of the southern hemisphere [Sánchez-
270 Lavega et al., 1996].

271

272 The 2018-2020 storms are probably responsible for the changes we report on the cloud-
273 field albedo (the two belts and the bright zone) that delineate the hexagon. However, the
274 dynamics of the hexagonal wave do not appear to have been strongly affected by the storm
275 activity, the wave remaining robust in the face of these threats. This is in agreement with the fact
276 that we did not observe changes in the polar wind profile. The mean rotation period of the
277 hexagon **in 2018-2020 was 10 h 39 min 21.1s \pm 2.8 s** (from Table 1). Since its discovery in 1980,
278 **the rotation period of the hexagon [Sánchez-Lavega et al., 2014; Hueso et al., 2020] has** perfectly
279 **matched the radio-rotation period (10 h 39 min 22.4 s; System III) measured at the time of**
280 **Voyager 1 and 2 [Desch and Kaiser, 1981] and used by the IAU [Archinal et al., 2018].** Recent
281 estimates of the yet undetermined Saturn's rotation period, based on a combination of gravity-
282 field measurements, zonal wind measurements and radio-occultations [Anderson and Schubert,
283 2007], on dynamical grounds [Read et al., 2009] and on ring seismology [Mankovich et al., 2019]
284 propose a shorter period than system III, of the order of 10 h 33 min. If this were the case, the
285 wind profile velocity relative to the new system would shift to lower values, and the speed of the
286 hexagonal wave would be -22 ms^{-1} instead of $\sim 0 \text{ ms}^{-1}$. This shift in the velocities does not affect
287 the Rossby wave model interpretation in Sánchez-Lavega et al. (2014).

288

289 The stability of the hexagon with respect to the nearby strong storms, together with **its long**
290 **lifetime** and **survival to** the strong seasonal insolation changes at its latitude, points towards a
291 meteorological formation with roots deep in Saturn's atmosphere, as proposed by some recent
292 models [Yadava and Bloxhama, 2020; Garcia et al., 2020]. This would be **consistent** with the deep
293 extension of the cloud top winds as deduced from gravity field measurements [Kaspi et al., 2020],
294 **reinforcing the idea of its possible relationship with the bulk rotation of the planet [Sánchez-**
295 **Lavega, 2005; Sánchez-Lavega et al., 2014].**

296
297
298
299
300
301
302
303
304
305
306
307
308
309
310
311
312
313
314
315
316
317
318
319
320
321
322
323
324
325
326
327
328
329
330
331
332
333
334
335
336
337

References

- Anderson, J. D. and Schubert, G (2007). Saturn's gravitational field, internal rotation, and interior structure, *Science* 317, 1384-1387.
- Antuñano, A., del Río-Gaztelurrutia T., Sánchez-Lavega A., and Hueso R. (2015). Dynamics of Saturn's polar regions, *J. Geophys. Res. Planets*, 120, 155–176, doi:10.1002/2014JE004709
- Antuñano A., del Río-Gaztelurrutia T., Sánchez-Lavega A., Rodríguez Aseguinolaza J. (2018). Cloud Morphology and Dynamics in Saturn's Northern Polar Region, *Icarus*, 299, 117-132.
- Archinal, B. A. et al. (2018) Report of the IAU working group on cartographic coordinates and rotation elements: 2015. *Celest. Mech. Dyn. Astr.* 130, 22.
- Baines, K. H., Delitsky, M. L., Momary, Th. W., Brown, R. H. , Buratti, B. J., Clark, R. N., Nicholson P. D. (2009). Storm clouds on Saturn: Lightning-induced chemistry and associated materials consistet with Cassini/VIMS spectra, *Planet. Space Sci.*, 57, 1650-1658.
- Cano, J. A. (1998) LAIA. Laboratorio de Análisis de Imágenes Astronómicas. Grup d'Estudis Astronòmics, Barcelona. Accessed 2020 at <http://www.ajax.ehu.es/Software/laia.html>
- del Río-Gaztelurrutia, T. et al. (2018). A planetary-scale disturbance in a long living three vortex coupled system in Saturn's atmosphere. *Icarus* 302, 499–513.
- Desch, M. D., and Kaiser L. M. (1981), Voyager measurements of the rotation period of Saturn's magnetic field, *Geophys. Res. Lett.*, 8, 253–256.
- Dyudina, U.A., Ingersoll A.P., Ewald S.P., Porco C.C., Fischer G., Kurth W., Desch M., Del Genio A., Barbara J., and Ferrier J. (2007). Lightning storms on Saturn observed by Cassini ISS and RPWS during 2004-2006, *Icarus*, 190, 545-555. doi:10.1016/j.icarus.2007.03.035.
- Garcia F., Chambers F. R. N. and Watts A. L. (2020). Deep model simulation of polar vortices in gas giant atmospheres, *Mont. Not. Roy. Astron. Soc.*, 499 (4), 4698–4715 doi.org/10.1093/mnras/staa2962
- García-Melendo, E., Pérez-Hoyos S., Sánchez-Lavega A. and Hueso R. (2011). Saturn's zonal wind profile in 2004–2009 from Cassini ISS images and its long-term variability. *Icarus* 215, 62–74.

338 García-Melendo E., Hueso R., Sánchez-Lavega A., Legarreta J., del Rio-Gaztelurrutia T., Pérez-
339 Hoyos S. and Sanz-Requena J. F. (2013), Atmospheric dynamics of Saturn's 2010 giant storm,
340 *Nature Geoscience* 6, 525–529
341
342 García-Melendo, E. & Sánchez-Lavega, A. (2017). Shallow water simulations of Saturn's giant
343 storms at different latitudes, *Icarus* 286, 241–260
344
345 Hueso, R. & Sánchez-Lavega, A. (2004). A three-dimensional model of moist convection for the
346 giant planets II: Saturn's water and ammonia moist convective storms. *Icarus* 172, 255–271.
347
348 Hueso R., Legarreta J., García-Melendo E., Sánchez-Lavega A. & Pérez-Hoyos S. (2009). The Jovian
349 anticyclone BA: II. Circulation and models of its interaction with the zonal jets, *Icarus*, 203, 499-
350 515.
351
352 Hueso R., Juaristi J., Legarreta J., Sánchez-Lavega A., Rojas J. F., Erard S., Cecconi B., Le Sidaner P.
353 (2018), The Planetary Virtual Observatory and Laboratory (PVOL) and its integration into the
354 Virtual European Solar and Planetary Access (VESPA), *Planet. Space Sci.*, 150, 22-35.
355
356 Hueso R., Sanchez-Lavega A., Rojas J. F., Simon A., Barry T., de Rio-Gaztelurrutia T., Sayanagi K.M.,
357 Antuñano A., Blalock J., Colas F., Delcroix M., Gomez-Forrellad J. M., Gunnarson J., Peach D.,
358 Perez-Hoyos S., Wong M. H., (2020). Saturn atmospheric dynamics one year after Cassini: Long-
359 lived features and hexagon's drift rate variations, *Icarus*, 336, 113429.
360
361 Kaspi Y., Galanti E., Showman A. P., Stevenson D. J., Guillot T., Iess L. and Bolton S. J., (2020).
362 Comparison of the Deep Atmospheric Dynamics of Jupiter and Saturn in Light of the Juno and
363 Cassini Gravity Measurements, *Space Sci. Rev.*, 216:84. doi.org/10.1007/s11214-020-00705-7
364
365 Mankovich Ch., Marley M. S., Jonathan J. F., and Movshovitz, N. (2019). Cassini Ring Seismology
366 as a Probe of Saturn's Interior. I. Rigid Rotation, *Astrophys. J.*, 871:1 (15pp)
367
368 Morales-Juberías R., Sayanagi K. M., Simon A. A., Fletcher L. N., Cosentino R. G. (2015),
369 Meandering shallow atmospheric jet as a model of Saturn's North-Polar hexagon, *Astrophys. J.*
370 *Let.*, 806, L18.
371
372 Read, P.L., Dowling, T. E. and Schubert, G. (2009). Saturn's rotation period from its atmospheric
373 planetary-wave configuration, *Nature* 460, 608-610.
374
375 Rostami M., Zeitlin V., Spiga A. (2017). On the dynamical nature of Saturn's North Polar hexagon,
376 *Icarus*, 297, 59-70.
377
378 Sánchez Lavega, A., Lecacheux J., Gomez J. M., Colas F., Laques P., Noll K., Gilmore D., Miyazaki
379 I. & Parker D. (1996). Large-scale storms in Saturn's atmosphere during 1994. *Science* 271, 631–
380 634
381

382 Sánchez-Lavega, A., Rojas J. F., and Sada P. V. (2000), Saturn's zonal winds at cloud level, *Icarus*,
383 147, 405–420.

384

385 Sánchez-Lavega, A. (2005), How long is the day on Saturn? *Science*, 307, 1223–1224.

386

387 Sánchez-Lavega A., del Río-Gaztelurrutia T., Hueso R., Gómez-Forrellad J.M., Sanz-Requena J. F.,
388 Legarreta J., García-Melendo E., Colas F., Lecacheux J., Fletcher L. N., Barrado-Navascués D.,
389 Parker D. and the International Outer Planet Watch team (2011), Deep winds beneath Saturn's
390 upper clouds from a seasonal long-lived planetary-scale storm, *Nature*, 475, 71-74.

391

392 Sánchez-Lavega A., del Río-Gaztelurrutia T., Hueso R., Pérez-Hoyos S., García-Melendo E.,
393 Antuñano A., Mendikoa I., Rojas J. F., Lillo J., Barrado-Navascués D., Gomez-Forrellad J. M., Go C.,
394 Peach D., Barry T., Milika D. P., Nicholas P., and Wesley A. (2014). The long-term steady motion
395 of Saturn's hexagon and the stability of its enclosed jet stream under seasonal changes, *Geophys.*
396 *Res. Lett.*, 41, 1425-1431.

397

398 Sánchez-Lavega A., Sromovsky L., Showman A., Del Genio A., Young R., Hueso R., García Melendo
399 E., Kaspi Y., Orton G. S., Barrado-Izagirre N., Choi D. & Barbara J., (2019). *Zonal Jets in Gas Giants*
400 chapter of the book *Zonal Jets*, pp. 9-45, eds. B. Galperin and P. Read, Cambridge University Press
401 (Cambridge, U.K.)

402

403 Sánchez-Lavega A., Fisher G., Fletcher L. N., Garcia-Melendo E., Hesman B., Perez-Hoyos S.,
404 Sayanagi K. & Sromovsky L., (2019). *The Great Storm of 2010-2011*, Chapter 13 of the book *Saturn*
405 *in the 21st Century*, pp. 377-416, eds. K. H. Baines, F. M. Flasar, N. Krupp, T. S. Stallard, Cambridge
406 University Press (Cambridge, U.K.)

407

408 Sánchez-Lavega, A., García-Melendo, E., Legarreta, J., Hueso, R., del Río-Gaztelurrutia, T., Sanz-
409 Requena, J. F., Pérez-Hoyos, S., Simon, A. A., Wong, M. H., Soria, M., Gómez-Forrellad, J. M.,
410 Barry, T., Delcroix, M., Sayanagi, K. M., Blalock, J. J., Gunnarson, J. L., Dyudina, U., Ewald, S., 2020.
411 A complex storm system in Saturn's north polar atmosphere in 2018. *Nature Astronomy* 4, 180-
412 187. Doi: 10.1038/s41550-019-0914-9.

413

414 Sanz-Requena, J. F., Pérez-Hoyos S., Sánchez-Lavega A., Antuñano A. & Irwin P. J. (2018). Haze
415 and cloud structure of Saturn's North Pole and Hexagon Wave from Cassini/ISS imaging. *Icarus*
416 305, 284–300.

417

418 Sayanagi, K., Baines, K., Dyudina, U., Fletcher, L., Sánchez-Lavega, A., & West, R. (2019). Saturn's
419 Polar Atmosphere, in *Saturn in the 21st Century*, pp. 337-376, K. Baines, F. Flasar, N. Krupp, & T.
420 Stallard (Eds.), Cambridge University Press (Cambridge, U. K.)

421

422 Simon A. A , Wong M. H and Orton G.S. (2015). First results from the Hubble OPAL program:
423 Jupiter in 2015, *Astrophys. J. Lett.*, 812, 55.

424

425 Simon A. A., Hueso R., Sánchez-Lavega A., Wong M. H. (2021). Mid-summer atmospheric changes
426 in Saturn's northern hemisphere from the Hubble OPAL program, *Planet. Sci. J.*, 2:47 (9pp)

427
428 Smith, B. A., Soderblom, L., Batson, R. M., Bridges, P. M., Inge, J. L., Masursky, H., Shoemaker, E.,
429 Beebe, R. F., Boyce, J., Briggs, G., Bunker, A., Collins, S. A., Hansen, C., Johnson, T. V., Mitchell, J.
430 L., Terrile, R. J., Cook, A. F., Cuzzi, J. N., Pollack, J. B., Danielson, G. E., Ingersoll, A. P., Davies, M.
431 E., Hunt, G. E., Morrison, D., Owen, T., Sagan, C., Veverka, J., Strom, R., and Suomi, V. E. (1982).
432 A new look at the Saturn system - The Voyager 2 images. *Science*, 215, 504-537.

433
434 Sromovsky, L. A., Revercomb H. E., Krauss R. J., & Suomi V. E. (1983). Voyager 2 observations of
435 Saturn's northern mid-latitude cloud features: morphology, motions, and evolution, *J. Geophys.*
436 *Res.* 88, 8650–8666

437
438 Yadava R. K. & Bloxhama J. (2020), Deep rotating convection generates the polar hexagon on
439 Saturn, *Proc. Nat. Acad. Sci.*, 117, 13991-13996. doi:10.1073/pnas.2000317117

440

441 **Acknowledgments**

442
443 This work has been supported by the Spanish project AYA2015-65041-P and PID2019-109467GB-
444 I00 (MINECO/FEDER, UE) and Grupos Gobierno Vasco IT1366-19. EGM is Serra Hunter Fellow at
445 UPC. This work has used data acquired from the NASA/ESA HST Space Telescope, which is
446 operated by the Association of Universities for Research in Astronomy, Inc., under NASA contract
447 NAS 5-26555. These HST observations are associated with program GO/DD 15262. EGM, MS, KAV
448 and ASL thankfully acknowledge the computer resources at Mare Nostrum and the technical
449 support provided by Barcelona Supercomputing Center (AECT-2019-2-0006). We thank all the
450 observers who have contributed with their images to the monitoring of the atmospheric activity
451 on Saturn during the years 2019 and 2020 and whose list and images can be found in the ALPO-
452 Japan and PVOL databases. Part of the amateur observations analyzed were obtained through a
453 collaboration with Europlanet 2024 RI. Europlanet 2024 RI has received funding from the
454 European Union's Horizon 2020 research and innovation program under grant agreement No
455 871149.

456
457

458 **Data availability**

459
460 The data that support the plots within this paper and other findings of this study are available at
461 the following repository (private access for editor and reviewers for evaluation):

462 <https://figshare.com/s/f39fcf055d3337997a01>

463 <https://doi.org/10.6084/m9.figshare.13546793>

464 The ground-based images included in the above repository have been downloaded from the
465 following sources:

466 Association of Lunar and Planetary Observers ALPO – Japan:

467 <http://alpo-j.sakura.ne.jp/Latest/Jupiter.htm>

468 PVOL2 database: <http://pvol2.ehu.eus/pvol2/>

469 Images from the HST-OPAL program are available at:
470 <https://archive.stsci.edu/prepds/opal/>
471 The image navigation software WinJupos is available at:
472 <http://jupos.org/gh/download.htm>
473 The image correlation software PICV can be accessed at:
474 <https://doi.org/10.5281/zenodo.4312675>
475 The shallow water model code can be accessed at:
476 <https://doi.org/10.5281/zenodo.4312681>